

# Simulations Approaching Data: Cortical Slow Waves in Inferred Models of the Whole Hemisphere of Mouse

Cristiano Capone<sup>1, \*</sup>, Chiara De Luca<sup>1, 7, \*</sup>, Giulia De Bonis<sup>1</sup>, Robin Gutzen<sup>5,6</sup>, Irene Bernava<sup>1</sup>, Elena Pastorelli<sup>1</sup>, Francesco Simula<sup>1</sup>, Cosimo Lupo<sup>1</sup>, Leonardo Tonielli<sup>1</sup>, Francesco Resta<sup>2</sup>, Anna Letizia Allegra Mascaro<sup>2,3</sup>, Francesco Pavone<sup>2,4</sup>, Michael Denker<sup>5</sup>, and Pier Stanislao Paolucci<sup>1</sup>

<sup>1</sup>INFN, Sezione di Roma

<sup>2</sup>LENS, Firenze, Italy

<sup>3</sup>CNR, Italy

<sup>4</sup>University of Florence, Physics Department, Italy

<sup>5</sup>Institute of Neuroscience and Medicine (INM-6) and Institute for Advanced Simulation (IAS-6) and JARA-Institute Brain Structure-Function Relationships (INM-10), Jülich Research Centre, Jülich, Germany

<sup>6</sup>Theoretical Systems Neurobiology, RWTH Aachen University, Aachen, Germany

<sup>7</sup>PhD Program in Behavioural Neuroscience, “Sapienza” University of Rome

\*These authors contributed equally to this work

May 26, 2022

## Abstract

Recent enhancements in neuroscience, like the development of new and powerful recording techniques of the brain activity combined with the increasing anatomical knowledge provided by atlases and the growing understanding of neuromodulation principles, allow studying the brain at a whole new level, paving the way to the creation of extremely detailed effective network models directly from observed data. Leveraging the advantages of this integrated approach, we propose a method to infer brain models capable of reproducing the complex spatio-temporal dynamics of the slow waves observed in the dorsal cortex of live mice under Ketamine-Xylazine anesthesia. To reliably claim the good match between data and simulations, we implemented a versatile ensemble of analysis tools, applicable to both experimental and simulated data and capable to identify and quantify the spatio-temporal propagation of waves across the cortex. Entering the details of the inference procedure we introduced, it is made up of two steps: the inner and the outer loop. First, in the inner loop, the parameters of a mean-field model are optimized by likelihood maximization, exploiting the anatomical knowledge to define connectivity priors. Then, the outer loop includes a periodic neuro-modulation and explores “external” parameters, seeking for an optimal match between the simulation outcome and the data, relying on observables (speed, direction, and frequency of the waves) apt for the characterization of cortical slow waves. We show that our model is capable to reproduce most of the features of the non-stationary and non-linear dynamics displayed by the extended cortical network. Also, the proposed method would allow, in principle, to identify the relevant modifications of parameters when the brain state changes, e.g. according to anesthesia levels. Finally, the interplay between experimental and simulated dynamics requested by the inference approach led to focus on robustness and generalizability in the development of data analysis tools, enlarging the scope of application of the introduced methodology.

# Introduction

In the last decade, large-scale optical imaging coupled with fluorescent activity indicators has provided new insights on the study of brain activity patterns [1, 21, 10, 45, 44, 16, 53, 50, 54]. The main tools currently employed to investigate neuronal activity at the mesoscale are Voltage Sensitive Dyes (VSDs) and Genetically Encoded Calcium Indicators (GECIs). Although there are a few studies that exploit the VSDs to explore the dynamics of cortical traveling waves during anesthesia [1, 44], the use of genetically encoded proteins presents important advantages. Indeed, GECIs are less invasive compared to synthetic dyes, allow repeated measures on the same subject and – more important – can be targeted to specific cell populations. GECIs are indirect reporter of neuronal activity by changing their relative fluorescence following the activity-dependent fluctuations in calcium concentration [29, 20], and the usage of GECIs to map spontaneous network activity has recently supplied important information about the spatio-temporal features of slow waves activity [53, 50]. Here, we considered experimental recordings obtained from Thy1-GCaMP6f transgenic mice, that express the GCaMP6f indicator in excitatory neurons, a widely used GECI characterized by a very high sensitivity and a fast dynamic response [10]. Despite the lower temporal resolution compared to state-of-the-art electrophysiological methods, the imaging approach that combines calcium indicators with wide-field microscopy increases both the spatial resolution and the specificity of the recorded neuronal population, thus appearing to be appropriate for our aim of modelling large-scale network dynamics.

The building of dynamic models requires to embody in a mathematical form the causal relationships between variables deemed essential to describe the system of interest; of course, the value of the model is measured by both its ability to match observations and its predictive power. The classical approach to this problem is constructive: parameters appearing in the model are assigned through a mix of insights from knowledge about the main architectural characteristics of the system to be modeled, experimental observations, and trial-and-error iterations. A more recent approach is to infer the model parameters by maximizing some objective function, e.g., likelihood, entropy, or similarity defined through some specific observable (e.g., functional connectivity). Following this route, a small number of models have been able to reproduce the complexity of observed dynamics from a single recording. However, most of the models are focused on the fMRI resting state recordings and on the reproduction of the functional connectivity[2]. However, to make use of such data it still requires new adaptable analysis tools capable to extract and characterized the emerging activity.

In this work, we address the complexity of the biological system, aiming at reproducing the dynamics observed in a whole cortical hemisphere of a mouse with a high number of recording sites displaying non-trivial slow waves propagation patterns. Indeed, the rich and detailed picture of the cortical activity offered by calcium imaging recordings allows for a deep investigation of the ongoing phenomena, enabling the construction of data-constrained simulations. The phenomenon under investigation is the spontaneous slow waves dynamics displayed by the cortex of a mouse under anesthesia. We considered raw imaging datasets made up of 10.000 pixels per frame at  $50\mu m \times 50\mu m$  spatial resolution; the selection of the cortical region of interest and a spatial coarse-graining step reduced the number of recording and modeling sites down to 1400 pixels with a spatial resolution of  $100\mu m \times 100\mu m$ , which is still a number of channels that is considerably larger than the 10 - 100 channels usually recorded with maybe multi-electrode recordings.

A major difficulty in assessing the goodness of inferred models is the impossibility to directly compare the parameters of the model with the elements of the biological system, that are usually unknown in their entirety. In order to fill the gap between experimental probing and mathematical description, the approach we adopted is to consider some essential features of the spontaneous activity and check whether they can be reliably reproduced by the proposed inferred model.

The large number of parameters in the system, together with limited-time duration of stationary in-vivo recordings (order few minutes, 6 recordings lasting 40 s each in our case), emphasizes the importance of using good priors, since the resulting inferred system might be underdetermined. A possible approach could be to make use of Structural Connectivity (SC) and Functional Connectivity (FC) atlases that, however, are affected by degeneracy and, for mice, the need of post-mortem processing [47, 28, 26]. Instead, in our approach, we exploited a minimal amount of generic anatomical knowledge: (1) the exponential decay characterizing the lateral connectivity [43] (or intra-area connectivity), together with a certain degree of anisotropy characterizing the slow waves propagation and (2) the evidence about the suppression of long-

range (inter-area) excitatory connectivity during the expression of cortical slow waves [32], while lateral connectivity is preserved. This led us to set up a connectivity prior, introduced in the model as elliptical exponentially-decaying connectivity kernels. This choice allows parametrizing the postsynaptic connections of a population of neurons (usually described by  $N$  independent parameters) with one analytic function, reducing the number of parameters for a model of  $N$  cortical pixels/populations, from  $O(N^2)$  down to  $O(N)$ .

A common problem in inferring a model is that it is only possible to constrain some of the observables, usually the average activity and the correlations between different sites [42, 5]. Indeed, it remains difficult to constrain other aspects of the spontaneously generated dynamics [40], e.g., the variety of shapes of the traveling wavefronts and the distribution of frequency of slow waves. Aware of this issue, we propose a two-step approach that we name *inner loop* and *outer loop*. In the inner loop, the model parameters are optimized by maximizing the likelihood of reproducing the dynamics displayed by the experimental data locally in time (i.e. only dependent by the previous iteration step). In the outer loop, the outcome of the simulation and the experimental data are compared via observables based on the statistics of the whole time course of the spontaneously generated dynamics. We developed a modular analysis procedure able to extract relevant observables, such as the distributions of frequency of occurrence, and speed and direction of propagation of the detected slow waves. The set of analysis tools is flexible enough to be applied to both the experimentally recorded and the simulated activity data, allowing a direct comparison between model and experiment. Parameters are adjusted to maximize the similarity between the original dynamics and the one of the generative model via an inference procedure. Specifically, we demonstrate that the inclusion of a time-dependent acetylcholinic neuro-modulation term [18] in the model enables a better match between experimental recordings and simulations inducing a variability in the expressed dynamics otherwise stereotyped. This additional term influences the excitability of the network along the simulation time course. The outer loop thus enables a quantitative search for optimal modulation.

In the following, the *Results* section presents the main elements of this work (for methodological details, see *Methods* section), and the *Discussion* section illustrates limitations and potentials of the approach we introduced, in particular, in relation with experiments, theoretical, and modeling perspectives.

## Results

We propose a two-step procedure to reproduce, in a data-constrained simulation, the spontaneous activity recorded from the mouse cortex during anesthesia. Here, we considered signals collected from the right hemisphere of a mouse, anaesthetized with a mix of Ketamine and Xylazine. The activity of excitatory neurons labeled with the calcium indicator GCaMP6f is recorded through wide-field fluorescence imaging, see Fig.1A. In this anesthetized state, the cortex displays slow waves from  $\simeq 0.25Hz$  to  $\simeq 5Hz$  (i.e., covering a frequency range that corresponds to the full  $\delta$  frequency band and extends a little towards higher frequencies). The waves travel across distant portions of the cortical surface, exhibiting a variety of spatio-temporal patterns.

The optical signal is highly informative about the activity of excitatory neurons. However, the GCaMP6f indicator, despite being “fast” compared to other indicators, has a slow response in time if compared to the timescale of the spiking activity of the cells (see Fig.1B–left). The impact on the observed experimental signature can be described as a convolution of the original signal with a low-pass transfer function eq. (2), resulting in a recorded fluorescence signal that exhibits a peak after about  $200ms$  from the onset of the spike, and a long-tailed decay [10] (see Methods, Experimental Data and Deconvolution section for details). To take into account this effect, we performed a deconvolution of the fluorescence signal (Fig.1B–top) to better estimate the firing rate of the population of excitatory neurons, i.e., the multi-unit activity, recorded by each single pixel (see Fig.1B–bottom).

We considered two sets of six acquisitions (each one lasting 40 s) collected from two mice. We characterized the slow waves activity defining a set of macroscopic local observables: local speed, direction, and inter-wave interval (IWI, see Methods for more details). Also, we used these observables to compare the spontaneous dynamics measured in experimental recordings with the one reproduced in simulated data.

In this work, we propose a two-step inference method. In the first step, the inner loop, the parameters of the model are inferred through likelihood maximization, Fig.1C–left, exploiting a set of known, still generic, anatomical connectivity priors [43] and assuming that mechanisms of suppression of long-range connectivity

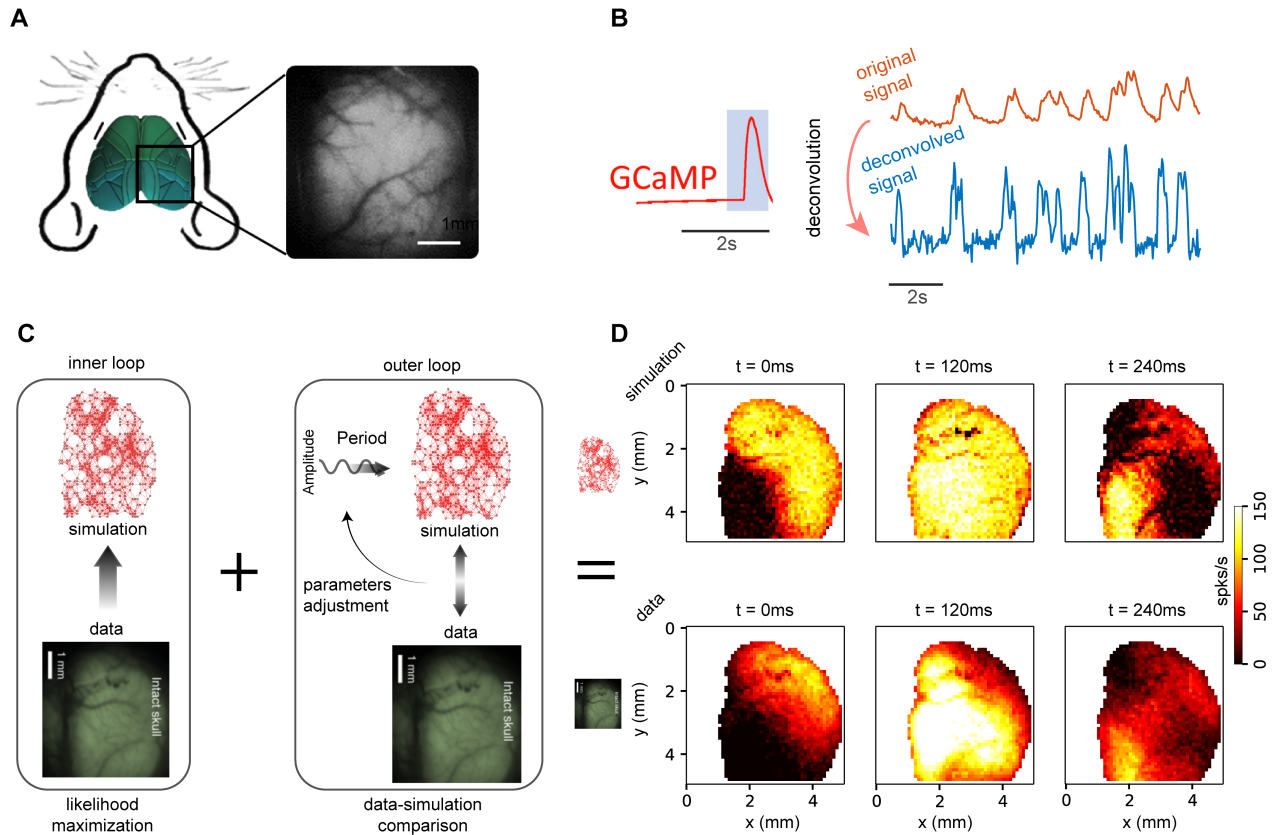


Figure 1: **Experimental setup and sketch of the model.** **A.** The cortical activity of the right hemisphere of a mouse (under Ketamine/Xylazine anesthesia) is recorded through wide-field calcium imaging (GCaMP6f indicator). **B.** The calcium indicator response is slow if compared with the time scales of neuron activity (top right). Applying a proper deconvolution function (left, an illustration; the actually applied transfer function is fitted from single-spike response [25, 10]), it is possible to estimate a good proxy for the average activity of the local population of excitatory neurons recorded by a single pixel (bottom right). **C.** Sketch of the inference model, made up of an inner loop (likelihood maximization) and an outer loop (search for optimal neuromodulation-related hyper-parameters granting the best match between simulations and data). **D.** Three frames from the simulation (top) and the experimental data (bottom), both expressing slow wave propagation.

are in action during the expression of global slow waves [32]. Such anatomical priors correspond to probabilities of connection among neuronal populations, and assume the shape of elliptical kernels exponentially decaying with the distance. For each pixel, the inference procedure has to identify the best local values for the parameters of such connectivity kernels. In addition, for each acquisition period  $tn \in \{t1, \dots, t6\}$ , it identifies the best local (i.e., channel-wise) values for spike-frequency-adaptation strength and external current.

In the second step, the outer loop, we seek for hyper-parameters (through a grid search exploration) granting the best match between model and experiment by comparing simulations and data, Fig.1C-right. This second step exploits acquired knowledge about neuro-modulation mechanisms in action during cortical slow waves expression, implementing them as in [18].

In Fig.1D, we provide a qualitative preview of the fidelity of our simulations by reporting three frames from the simulation (top) and the data (bottom). This example shows similarities in the slow waves propagation: the origin of the wave, the wave extension and the activity are qualitative comparable, as well as the activation pattern. A quantitative comparison is detailed in following sections.

## Characterization of the Cortical Slow Waves

In the framework of the activity we are carrying out in the Human Brain Project, aiming at the development of a flexible and modular analysis pipeline for the study of cortical activity [22] (see also [46]), we developed for this study a set of analysis tools applicable to both experimental and simulated data, capable to identify wavefronts and quantify their features.

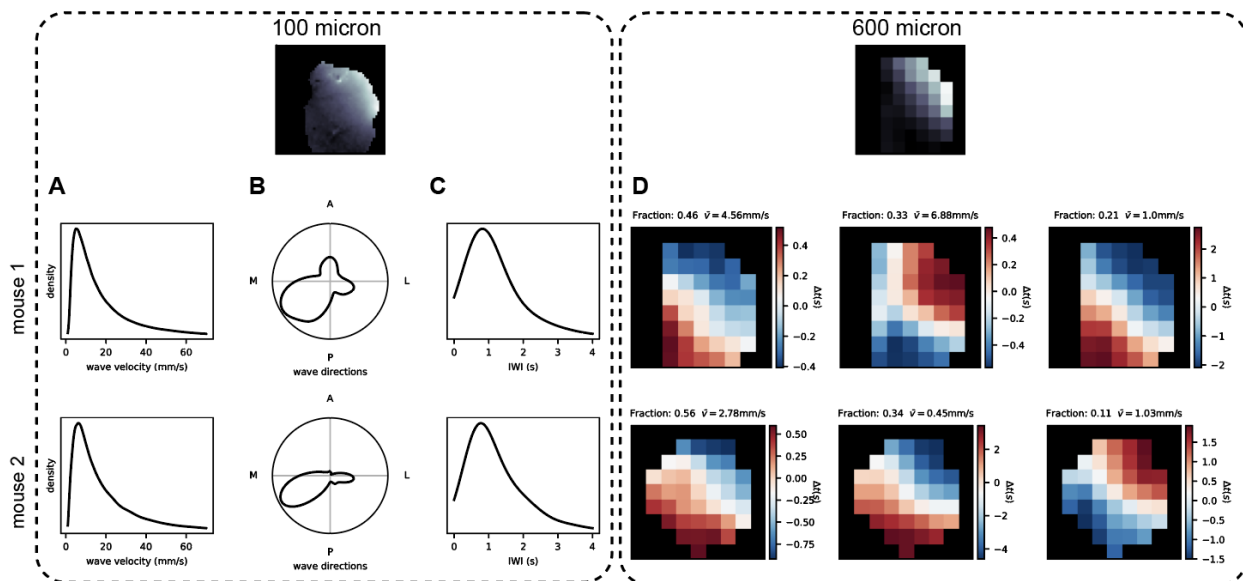


Figure 2: **Summary of wave propagation properties in experimental trials for two different mice.** Measures for the quantitative characterization and comparison of waves accumulated across all pixels and all trials in mouse 1 (upper row) and 2 (lower row), respectively. **A.** Local wave velocity distributions. **B.** Local wave direction distributions. **C.** Local inter-wave interval distributions. **D.** Wave propagation modes identified by Gaussian Mixture Model (GMM). The GMM classification algorithm returns the optimal number of clusters appropriate for grouping the waves identified in the observed dataset, then assigning each wave to a cluster, assuming each cluster is described by a multivariate gaussian distribution in the channel space (with its mean and covariance matrix). Distributions in panels A, B and C are at the original resolution (100  $\mu\text{m}$ ), while before application of GMM the channel-space dimension has been reduced to 600  $\mu\text{m}$  (see the original resolution compared to the downsampled one on top of the main panels). In the experimental data, three different wave propagation modes for each mouse are identified. The spatio-temporal propagation dynamics of each mode is normalized to the temporal center of each wave (from blue to red pixels).

Specifically, we improved the methodology implemented by [9] (see Methods for details), providing three quantitative local (i.e., channel-wise) measurements to be applied in order to characterize the identified slow waves activity: local wave velocity, local wave direction, and local wave frequency. The high spatial resolution of the data allows not only to extract global information for each wave, but also to evaluate the spatio-temporal evolution of the local observables within each wave.

For each channel participating in a wave event, the local velocity is evaluated as the inverse of the absolute value of its passage function gradient (see equation 21), the local direction is computed from the weighted average of the components of the local wave velocities (see equation 22), and the local wave frequency is expressed through its reciprocal, the inter-wave interval (IWI) evaluated from the duration between two consecutive waves passing through the same channel (see equation 23).

In Fig.2A-C we show a summary of the data analysis performed on all the recordings of the two mice. Interestingly, the defined experimental observables are remarkably comparable among the two subjects.

Further, we classified the waves into propagation modes with a Gaussian Mixture Model (GMM) classification approach applied in a downsampled channel space (44 and 41 informative channels for the two mice respectively) to identify the number of wave modes and cluster observed waves according to them. In Fig. 2D we report the wave propagation modes identified through GMM (see details in Methods, Gaussian Mixture Model section). Coherently with what expected from previous studies [35], in both mice two main propagation directions are identified: a more frequent antero-posterior and a less frequent postero-anterior direction.

## Two-step inference method

### The Inner Loop

The first step of our inference method can be seen as a one-way flow of information from data to model and consists of estimating model parameters by a likelihood maximization, see Fig3A.

We built a generative model as a network of interacting populations, each of them composed of 500 AdEx (Adaptive Exponential integrate-and-fire) neurons. Each population is modeled by a first-order mean-field equation [15, 17, 6, 4], according to which all the neurons in the population are described by their average firing rate. The neurons are affected by spike frequency adaptation, that is accounted for by an additional equation for each population (see Methods for details). We remark that we considered current-based neurons; however, the mean-field model might be extended to the conductance-based case [14, 8]. The single population aims at modeling the group of neurons recorded by a single pixel (the number of considered pixels, i.e. populations, is that obtained after the under-sampling is performed, as illustrated in Methods).

Single-neuron parameters (such as membrane potential, threshold, and so on) are assumed, with adopted values reported in TABLE I of Methods section. The other parameters (connectivity, external currents and adaptation) are inferred from the data. This is achieved by defining the log-likelihood  $\mathcal{L}$  for the parameters  $\{\xi\}$  to describe a specific observed dynamics  $\{S\}$  (see Methods section for details) as:

$$\mathcal{L}(\{S\}|\{\xi\}) = \sum_{i,t} \left[ -\frac{(S_i(t+dt) - F_i(t))^2}{2c^2} \right] \quad (1)$$

where  $F_i(t)$  is the transfer function of the population  $i$  and  $c$  is the variance of the Gaussian distribution from which the activity is extracted (see Methods). We remark that in this work we consider populations composed of excitatory/inhibitory neurons. To model this, it is necessary to use an effective transfer function describing the average activity of the excitatory neurons and accounting for the effect of the inhibitory neurons (see Methods for details, *Excitatory-Inhibitory module, the effective transfer function* section).

The optimal values for the parameters are inferred from maximizing the likelihood with respect to the parameters themselves. The optimizer we used is iRprop, a gradient-based algorithm [23]. The parameters are not assumed to be homogeneous in the space, and each population (identified by a pixel in the image of the cortex) is left free to have different inferred parameters. The resulting parameters can thus be reported in a map, as illustrated in Fig.3B,C,D,E,F,G. Each panel represents, color-coded, the spatial map of a different inferred parameter, describing its distribution over the cortex of the mouse. Specifically, 1)  $\lambda$ ,  $k_0$ ,

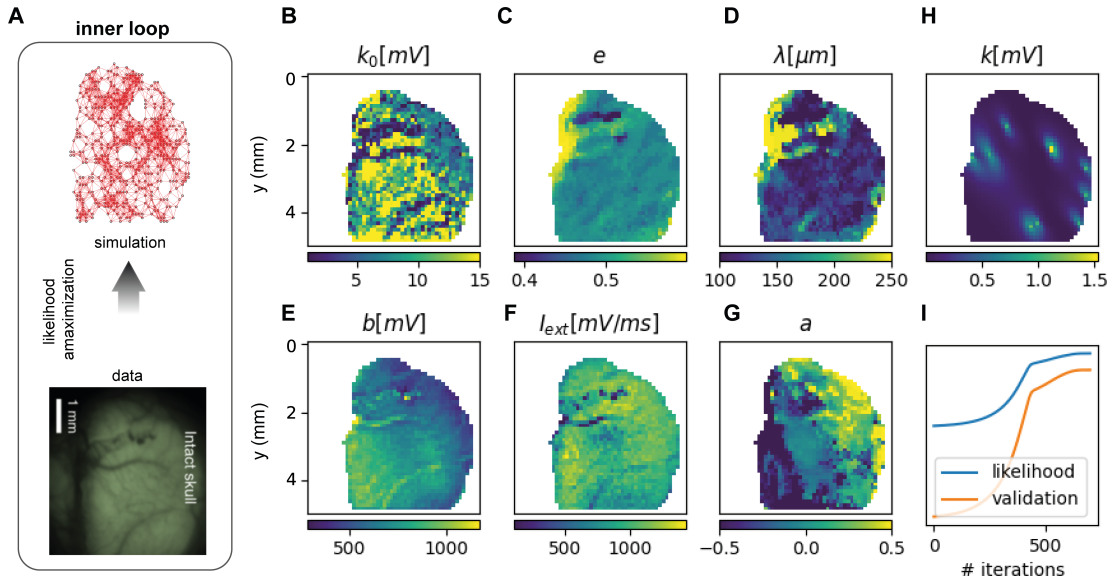


Figure 3: **Inner Loop.** **A.** The inner loop: likelihood maximization. **B,C,D,E,F,G.** Spatial maps of estimated parameters after 700 iterations of iRprop [24], that we further improved by setting priors for the expected spatial decay law of lateral connectivity. Parameters  $k_0$ ,  $e$ ,  $\lambda$ , and  $a$  are the connectivity parameters (weight, eccentricity, spatial scale, and anisotropy), as defined in Methods;  $I_{ext}$  and  $b$  are the local external input and the strength of the spike frequency adaptation strength. **H.** Ten inferred elliptic connectivity kernels, presented in an overlaid manner, that illustrates the existence of strong eccentricity  $e$  for the elliptic connectivity kernels. **I.** Training likelihood and validation likelihood (in blue and orange, respectively) as a function of the number of iterations.

$e$ ,  $a$  are the parameters that characterize at a local level the inferred shape of the elliptical exponentially-decaying connectivity kernels (see *Methods*, section *Elliptic exponentially-decaying connectivity kernels*); 2)  $b$  is the strength of the spike frequency adaptation (see section *Generative Model* and Eq.4); 3)  $I_{ext}$  is the local external input current. Panel **H** in Fig.3 presents, for a few exemplary pixels, the total amount of connectivity incoming from the surrounding region, and confirms the presence of a strong eccentricity ( $e$ ) and prevalent orientations ( $\phi$ ) for the elliptic connectivity kernels, elements that contribute to the initiation and propagation of wave-fronts along preferential axes, orthogonal to the major axis of the ellipses.

In principle, such inferred parameters define the generative model which reproduce at best the experimental data. A major risk while maximizing the likelihood (see Fig.3 **I**, blue line) is the over-fitting, which we avoid by considering the validation likelihood (see Fig.3 **I**, orange line), i.e. the likelihood evaluated on data expressing the same kind of dynamics but not used for the inference. A likelihood increase associated to a validation likelihood decrease during the inference procedure is an alarm for over-fitting, that we do not see in our case.

## The Outer Loop

The likelihood maximization (*inner loop*) constrains the dynamics at the following time step, given the activity at the previous step. Therefore, we expect that running a simulation with the inferred parameters should give a good prediction of the activity of the network. However, it is not straightforward that the spontaneous activity generated by the model would reproduce the desired variety of dynamical properties observed in the data. Indeed, the constraints imposed within the *inner loop* are local in time (i.e., the constraint at a certain time step  $t$  only depends on the state of the network at the previous time step  $t - 1$ ). As a consequence, the model is not able to generate the long-term temporal richness observed in data.

Specifically, we run the spontaneous mean-field simulation for the same duration of the original recording. We found that parameters estimated in the *inner loop* can be adopted to obtain a generative model capable to reproduce oscillations and traveling wavefronts. However, the activity produced by the model inferred from the *inner loop* results to be much more regular if compared to the experimental one. For instance, the down state duration and the wavefront shape express almost no variability when compared to experimental recordings.

For this reason, it is necessary to introduce the *outer loop* here described (see Figure 3A). First, we analyze the spontaneous activity of the generative model and compare it to the data, to tune the parameters that cannot be optimized by direct likelihood differentiation (see Fig.3A). Thus, we include in the model an external oscillatory neuro-modulation (inspired by [18]), and we look for optimal amplitude and period for such neuromodulation proxy, expected to affect both the values of  $I_{ext}$  and  $b$  (more details in Methods section).

The identification of the optimal values for these parameters requires the definition of a quantitative *score* to evaluate the similarity between data and simulation. Specifically, we opted for a quantitative comparison between the cumulative distributions of the three local observables characterizing the identified travelling waves (speed, direction and IWI, already introduced in Section Characterization of the Cortical Slow Waves) through the Earth Mover’s Distance (EMD, see Methods section for more details). The combination of such distances as a function of the two hyper-parameters (amplitude and period) leads to the identification of the optimal point (where the “Combined Distance” is minimal). Figure 4D depicts the results of this tuning on a single trial. The comparison between experimental and simulated cumulative macroscopic distributions for a “good” (optimal match) and a “bad” (non-optimal match) point in the grid search is depicted in panels **B** and **C**, respectively. We applied the procedure to both mice, 6 recorded trials, and calibrated the model on each trial independently. Optimal values for amplitude and period for each of them are depicted in Figures 4F and **G**, respectively. In panel **H**, on the other hand, the span of combined EMD measurements for each trial in both mice is shown (within the range of values for amplitude and period considered in the grid search), depicting the variety of the observed phenomena.

## Validation of the simulation through GMM-based propagation modes

As shown in Fig. 5, the sequential application of the inner and the outer loop (i.e., the two-step inference model) results in an evident improvement of the simulation. Specifically, when looking at the raster plot,

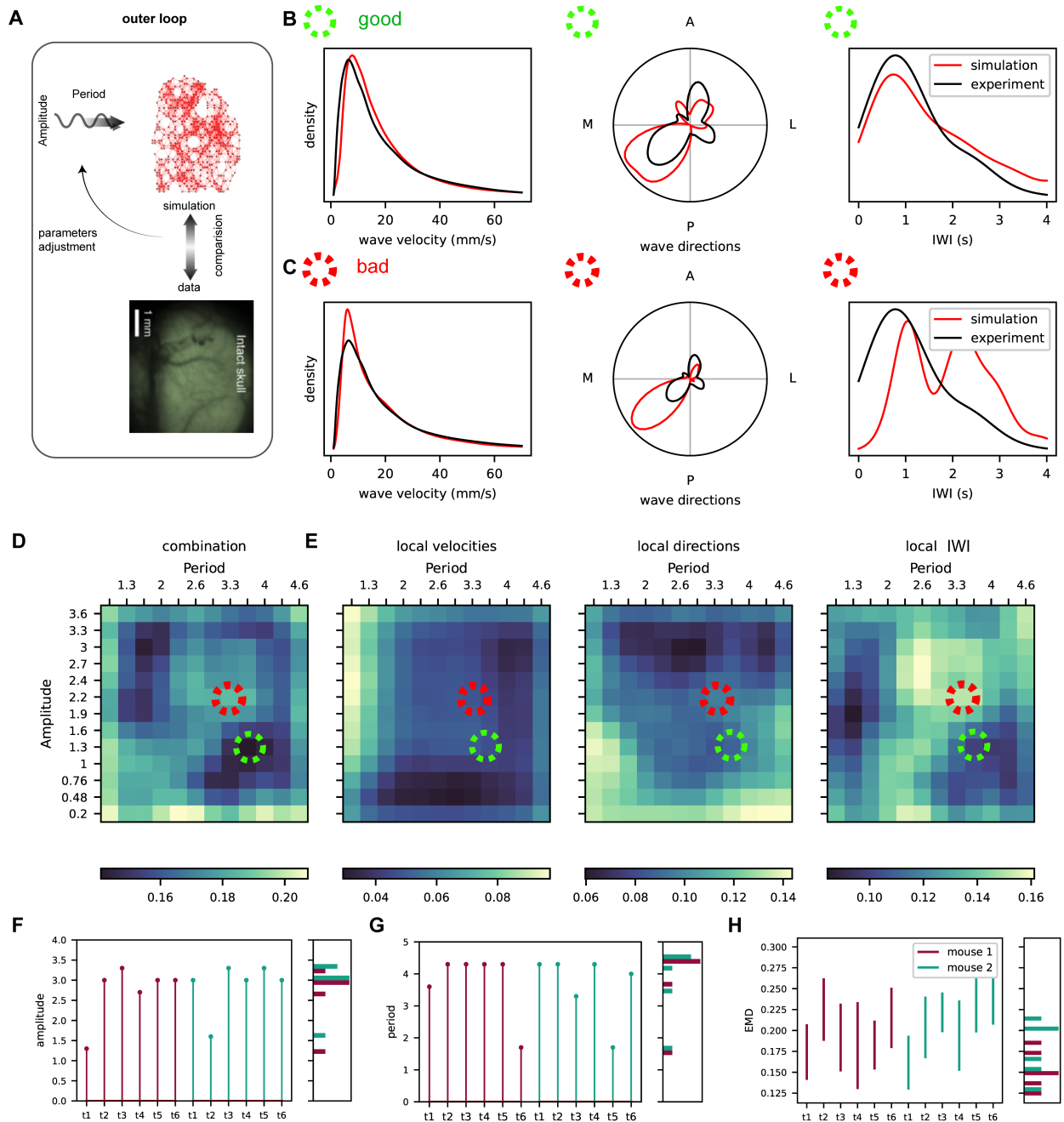


**Figure 4: Outer Loop.** **A.** The second step of the inference method consists in comparing simulations and data, to optimize neuromodulation amplitude and period hyper-parameters. Here, we have a bi-directional flow of information from data to model and the other way round. **B.** Direct comparison of the distributions of velocity (left panel), waves direction (central panel), and IWI (right panel) between data and simulation. The simulation is obtained selecting the optimal point (i.e. the minimum “combined distance” between experimental and simulated distributions) for the hyper-parameters grid search (amplitude and period of the neuromodulation signal, see panel D). **C.** Same as panel B, but for a non-optimal point of the grid search (see panel D). **D.** Results of the hyper-parameters grid search on a single trial. “Combined Distance” between simulated and experimental distributions (see text for details) is plotted as a function of the two hyper-parameters (amplitude and period). **E.** EMD between experimental and simulated distributions of velocities (left), directions (center) and IWI (right), for the same single trial of panel D. **F-G.** Summary (across trials, and for the two different mice) of optimal hyper-parameter values obtained from the grid search. **H.** Summary for the minimal and maximal “Combined Distance” for all the trials of the two mice, for the grid search in the same ranges of amplitude and period values of panel D.

the neuromodulation (outer loop) appears to be a key ingredient able to reduce the level of stereotypization of the wave collection, and to introduce elements that mimic the richness and variability of the biological phenomenon.

To further stress out this aspect, we introduce a color code for labeling waves belonging to the different clusters identified as distinct propagation modes by GMM when the model is applied to the collection of experimental waves. Indeed, besides illustrating the propagation features of the wave collections (as in Fig. 2), we use GMM as a tool for posterior validation of the simulation outcome (Fig. 6). The idea behind this approach is that GMM, acting on a wave collection, is able to identify distinct clusters, grouping wave events with comparable spatio-temporal features, if each identified cluster is significantly populated. This happens if the wave collection to which the GMM is applied for fitting the propagation modes is auto-consistent, i.e. contains propagation events that represent instances of the same coherent phenomenon.

Results reported in Fig. 6 suggest this interpretation: here, for each mouse, the wave collection to which the GMM is applied is made up by putting together wave events from the six experimental trials and wave events from the corresponding simulated trials. GMM acting on the entire collection (experiments + simulations) identifies 4 propagation modes; despite differences between the two mice, results illustrated in the pie charts show that the GMM is “fooled” by the simulation, meaning that the clustering process on the entire collection does not trivially separate experimental from simulated events. Or rather, experimental and simulated waves are nicely mixed when events are grouped in clusters identified by the GMM, implying a correspondence between data and simulations. Conversely, when the wave collection is constructed piling up experimental waves and events obtained by “shuffling” the output of the simulation, results of the GMM report a segregation between data and numerical events, suggesting that the GMM is not deceived by a simulation that is properly approaching the data. This case is explored in Supplementary Materials.

In other words, we can claim that data and simulations obtained from the two-step inference model here presented express the same propagation modes (centroids), while the expressed modes are orthogonal for a control case (the shuffled simulation).

## Discussion

In recent years, the field of statistical inference applied to neuronal dynamics has mainly focused on the reliable estimate of an effective synaptic structure of a network of neurons [41, 49, 31]. In [37] the authors demonstrated, on an in-vitro population of ON and OFF parasol ganglion cells, the ability of a Generalized Linear Model (GLM) to accurately reproduce the dynamics of the network [33]; in addition they studied the response properties of lateral intraparietal area neurons at the single-trial, single-cell level. The capability of GLM to capture a broad range of single neuron response behaviors was analyzed in [52]. However, in these works, the focus was on the response of neurons to stimuli of different spatio-temporal complexity. Moreover, recurrent connections, even when accounted for, did not provide a decisive correction to the network dynamics. A very few published studies to date have focused on the spontaneous dynamics of networks inferred from neuronal data. Most of them focused on the resting state recorded through fMRI and on the reproduction of its functional connectivity [2]. In [3] the temporal and spatial features of bursts propagation have been accurately reproduced, but on a simpler biological system, a culture of cortical neurons recorded with a 60 electrodes array. Here we aim at reproducing the dynamics of the whole hemisphere of the mouse with approximately 1400 recording sites.

One of the major risks when inferring a model is the failure of the obtained generative model to reproduce a dynamics comparable to the data. The reason for this is the difficulty to constrain some of the observables when inferring a model. A common example is offered by the Ising model: when inferring its couplings and external fields, only magnetizations and correlations between different spins are constrained [42], but it is not possible to constrain the power spectrum displayed by the model and other temporal features. When this experiment is done on the Ising model itself, this is not a problem: if the dataset is large enough, the correct parameters are inferred and also the temporal features are correctly reproduced. However, if the original model contains some hidden variables (unobserved neurons, higher-order connectivities, other dynamical variables), the dynamics generated by the inferred model might not be representative of the original dynamics. This led us to introduce the two-step method, in order to adjust parameters beyond likelihood maximization.

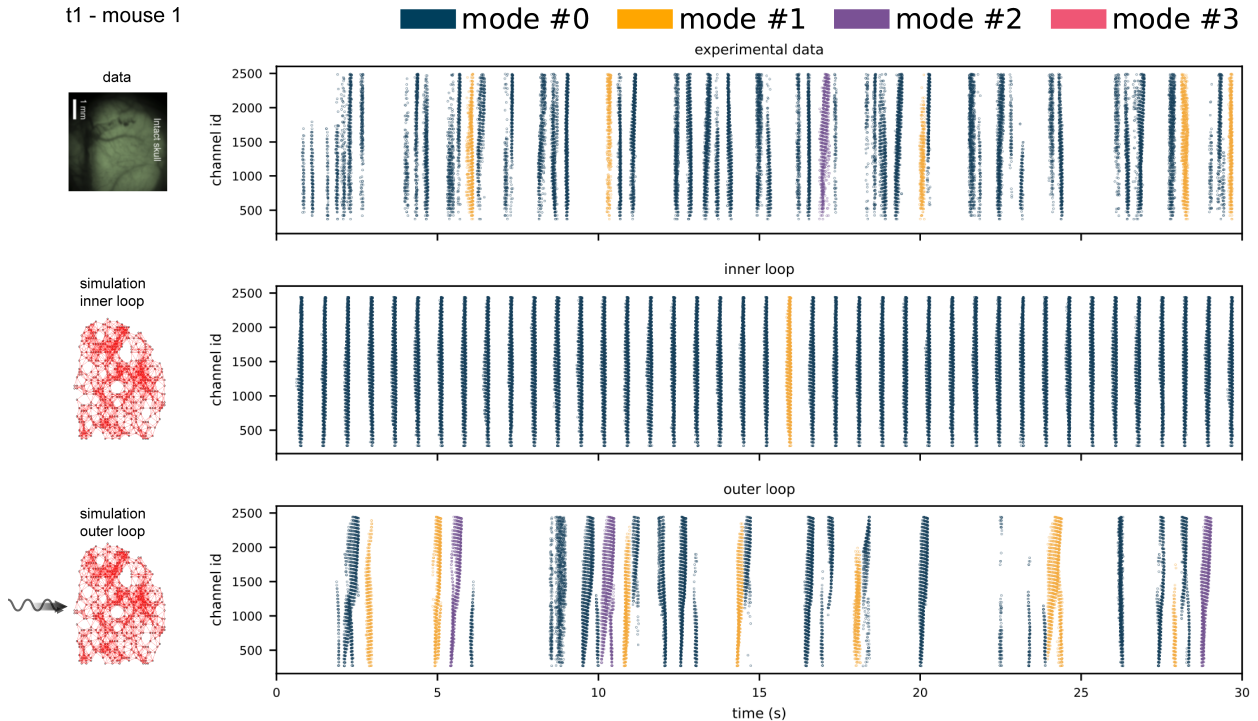


Figure 5: **Dynamics comparison.** Raster plot of the detected waves in experimental data (top), in simulated data without neuromodulation (output of the inner loop, center), and in simulated data with optimal neuromodulation (output of the outer loop, bottom). For visualization purposes, only 30s out of the 40s of the recording (mouse 1, trial 1) are reported. All the waves detected in the three scenarios are classified through a GMM approach; the four GMM modes are identified from fitting the collection of experimental + simulated waves. Wave colors indicate the modes of propagation.

Another obvious but persisting problem in the application of inference models to neuroscience has been how to assess the value of inferred parameters, as well as their biological interpretation. In the literature, a cautionary remark is usually included, recognizing that inferred couplings are to be meant as ‘effective’, leaving of course open the problem of what exactly this means.

One way to infer meaningful parameters is to introduce good priors. In this work we assumed that under anesthesia the inter-areal connectivity is largely suppressed in favor of lateral connectivity, as demonstrated e.g. in [32] during a similar oscillatory regime. Also, the probability of lateral connectivity in the cortex is experimentally known [43] to decay with the distance according to an exponential shape, with a spatial scale in the range of a few hundreds of  $\mu m$ . Furthermore, the observation of preferential directions for the propagation of cortical slow waves [7] suggested us to explicitly account for such anisotropy. For all of these reasons, we introduced exponentially decaying elliptical connectivity kernels in our model. We remark that inferring connections at this mesoscopic scale allows obtaining information complementary to that contained in inter-areal connectivity atlases, where connectivity is considered on a larger spatial scale and it is carried by white matter rather than by lateral connectivity.

A key feature of neural networks is *degeneracy*, the ability of systems that are structurally different to perform the same function [47]. In other words, the same task can be achieved by different individuals with different neural architectures. However, generic atlases of Structural Connectivity (SC) and Functional Connectivity (FC) contain information averaged among different individuals. Though similar functions and dynamics can be sustained in each individual by referring to specific SCs and FCs [28, 26], detailed information about individual brain peculiarities are lost with this approach. In the framework here presented, detailed individual connectivities can be directly inferred *in vivo*, contributing to the construction of brain-specific models descriptive of the dynamical features observed in one specific individual.

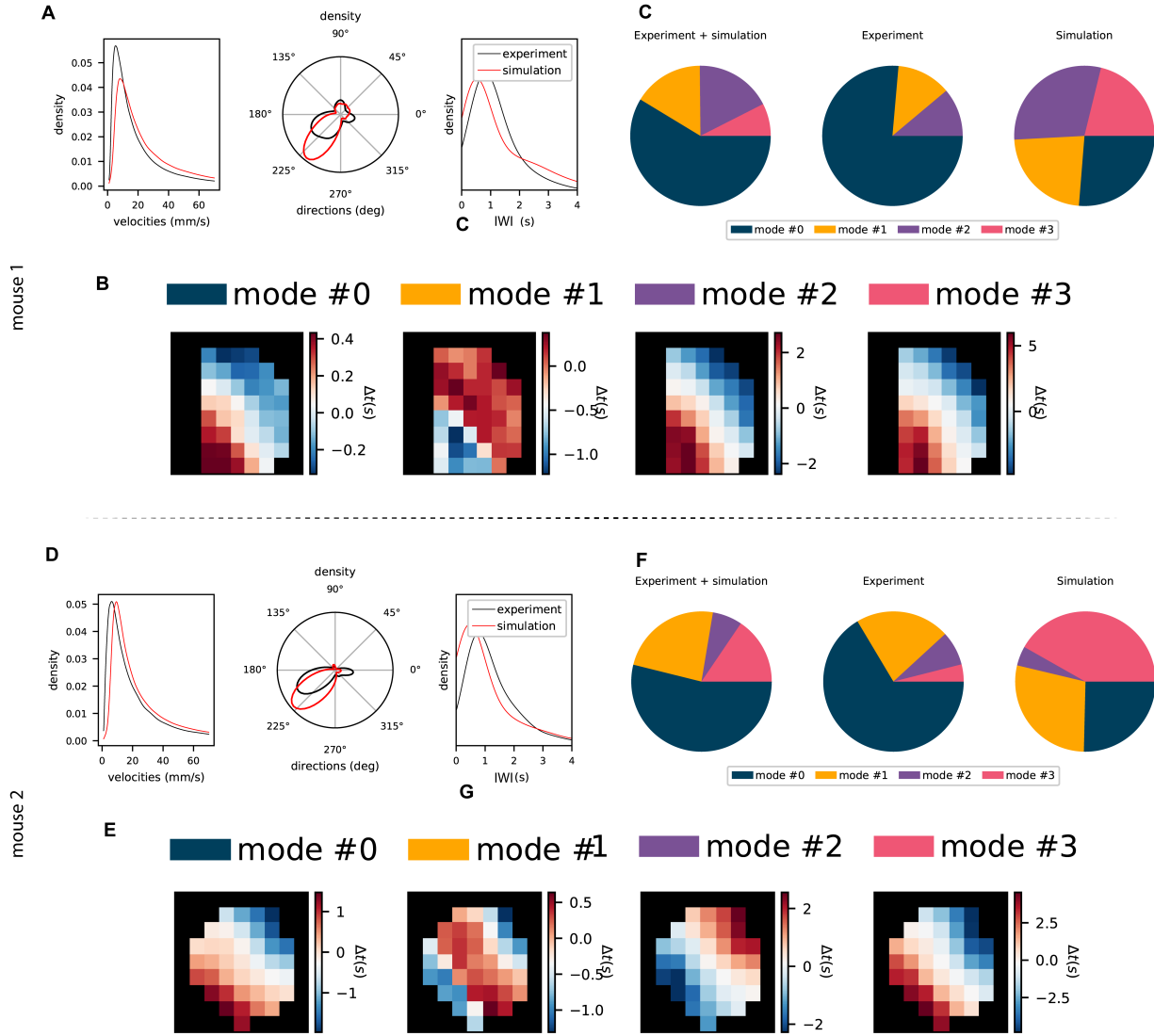


Figure 6: **Validation of propagation modes.** Analysis over the full set of 6 experimental trials and corresponding optimal simulations (for each of the two mice). Optimal simulations are selected trial-wise following the grid search approach, as described in section The Outer Loop. **A** and **D**. Direct comparison between experimental and simulated distributions of wave velocity (left panel), direction (central panel), and IWI (right panel). **B** and **E**. Centroids of the 4 gaussian distributions (modes) in the downsampled channel space describing the collection of experimental and simulated waves fitted with the GMM. **C** and **F**. Fraction of each of the detected modes in the full collection (experiments and simulations, left), in the sub-collection of experiments only (center), and simulations only (right).

One of the values added by the modeling technique here described is that its dynamics relies on a mean-field theory which describes populations of interconnected spiking neurons. This is particularly useful to set up a richer and more realistic dynamics in large-scale spiking simulations of slow waves and awake-like activity [34], that in absence of such detailed inferred parameters behave according to quite stereotyped spatio-temporal features.

In perspective, we plan to integrate plastic cortical modules capable of incremental learning and sleep on small-scale networks with the methodology here described, demonstrating the beneficial effects of sleep on

cognition [6, 19].

Finally, we plan to go beyond spontaneous activity, aiming at modeling the dynamics of the network when it receives input signals, ranging from simple (local) electrical perturbations to sensory stimuli. The methodology to achieve this would be very similar to what presented in [30, 13].

## Methods

### Mouse wide-field calcium imaging

*In vivo* calcium imaging datasets have been acquired by LENS personnel (European Laboratory for Non-Linear Spectroscopy<sup>1</sup>) in the Biophotonics laboratory of the Physics and Astronomy Department, Florence, Italy. All the procedures were performed in accordance with the rules of the Italian Minister of Health (Protocol Number 183/2016-PR). Mice were housed in clear plastic enriched cages under a 12 h light/dark cycle and were given *ad libitum* access to water and food. The transgenic mouse line C57BL/6J-Tg(Thy1GCaMP6f)GP5.17Dkim/J (referred to as GCaMP6f mice<sup>2</sup>) from Jackson Laboratories (Bar Harbor, Maine USA) was used. This mouse model selectively expresses the ultra-sensitive calcium indicator (GCaMP6f) in excitatory neurons.

Surgery procedures and imaging: 6-month old male mice were anaesthetized with a mix of Ketamine (100 mg/kg) and Xylazine (10 mg/kg). The procedure for implantation of a chronic transcranial window is described in [9]. Briefly, to obtain optical access to the cerebral mantle below the intact skull, the skin and the periosteum over the skull were removed following application of the local anesthetic lidocaine (20 mg/mL). Imaging sessions were performed right after the surgical procedure. Wide-field fluorescence imaging of the right hemisphere were performed with a 505 nm LED light (M505L3 Thorlabs, New Jersey, United States) deflected by a dichroic mirror (DC FF 495-DI02 Semrock, Rochester, New York USA) on the objective (2.5x EC Plan Neofluar, NA 0.085, Carl Zeiss Microscopy, Oberkochen, Germany). The fluorescence signal was selected by a band-pass filter (525/50 Semrock, Rochester, New York USA) and collected on the sensor of a high-speed complementary metal-oxide semiconductor (CMOS) camera (Orca Flash 4.0 Hamamatsu Photonics, NJ, USA). A 3D motorized platform (M-229 for the *xy* plane, M-126 for the *z*-axis movement; Physik Instrumente, Karlsruhe, Germany) allowed the correct subject displacement in the optical setup.

### Experimental Data and Deconvolution

We assume that the optical signal  $X_i(t)$  acquired from each pixel  $i$  is proportional to the local average excitatory (somatic and dendritic) activity (see Fig.1). The main issue is the slow (if compared to the spiking dynamics) response of the calcium indicator (GCaMP6f). We estimate the shape of such a response function from the single spike response [10] as a log-normal function:

$$\text{LN} \left( \frac{t}{dt}; \mu, \sigma \right) = \frac{dt}{t} \frac{1}{\sqrt{2\pi}\sigma} \exp \left( -\frac{(\ln \frac{t}{dt} - \mu)^2}{2\sigma^2} \right), \quad (2)$$

where  $dt = 40ms$  is the temporal sampling frequency, and  $\mu = 2.2$  and  $\sigma = 0.91$  have been estimated in [9]. We assume a linear response of the calcium indicator (which is known to be not exactly true [10]) and we apply the deconvolution to obtain an estimation of the actual firing rate time course  $S_i(t)$ . The deconvolution is achieved by dividing the signal by the lognormal in the Fourier space:

$$\hat{S}_i(k) = \frac{\hat{X}_i(k)}{\hat{LN}(k)} \Theta(k_0 - k) \quad (3)$$

where  $\hat{X}_i(k) = \text{fft}(X_i(t))$  and  $\hat{LN}(k) = \text{fft}(\hat{LN}(t))$  ( $\text{fft}(\cdot)$  is the fast Fourier transform). Finally, the deconvolved signal is  $S_i(t) = \text{ifft}(\hat{S}_i(k))$  ( $\text{ifft}(\cdot)$  is the inverse fast Fourier transform). The function  $\Theta(k_0 - k)$  is the Heaviside function and is used to apply a low pass filter with a cutoff frequency  $k_0 = 6.25Hz$ .

<sup>1</sup>LENS Home Page, <http://www.lens.unifi.it/index.php>

<sup>2</sup>For more details, see The Jackson Laboratory, Thy1-GCaMP6f, <https://www.jax.org/strain/025393>.

## Generative Model

We assume a system composed of  $N_{pop}$  (approximately 1400, as the number of pixel) interacting populations of neurons. The population  $j$  at time  $t$  has a level of activity (firing rate) defined by the variable  $S_j(t) = \{0, 1, 2, \dots\}$ . As anticipated, each population  $j$  is associated to a pixel  $j$  of the experimental optical acquisition, and contains  $N_j$  neurons;  $J_{ij}$  and  $C_{ij}$  are the average synaptic weight and the average degree of connectivity between populations  $i$  and  $j$ . We define the parameter  $k_{ij} = N_j J_{ij} C_{ij}$  as the relevant one in the inference procedure. We also consider that each population receives an input from a virtual external populations composed of  $N_j^{ext}$  neurons, each of which injecting a current  $J_j^{ext}$  in the population with a frequency  $\nu_j^{ext}$ . Similarly to what was done above, we define the parameter  $I_j^{ext} = \nu_j^{ext} N_j^{ext} J_j^{ext}$ .

In a common formalism, site  $i$  at time  $t$  is influenced by the activity of other sites through couplings  $k_{ik}$  [3], in terms of a local input current defined as

$$\mu_i(t) = \sum_k k_{ik} S_k(t) + I_i^{ext} - b_i W_i(t) \quad (4)$$

The term  $b_i W_i(t)$  accounts for a feature that plays an essential role in modeling the emergence of cortical slow oscillations: the spike frequency state-dependent adaptation, that is the progressive tendency of neurons to reduce their firing rates even in the presence of constant excitatory input currents. Spike frequency adaptation (SFA) is known to be much more pronounced in deep-sleep and anaesthesia than during wakefulness. From a physiological stand-point, this is associated to the calcium concentration in neurons and can be modeled introducing a negative (hyper-polarizing) current on population  $i$  (the  $b_i W_i(t)$  term in eq.4).

$W(t)$  is the adaptation variable: it increases when a neuron  $i$  emits a spike and is gradually restored to its rest value when no spikes are emitted; its dynamics can be written as

$$W_i(t + dt) = (1 - \alpha_w) W_i(t) + \alpha_w S_i(t + dt) \quad (5)$$

where  $\alpha_w = 1 - \exp(-dt/\tau_w)$ , and  $\tau_w$  is the characteristic time scale of SFA.

It is also customary to introduce the adaptation strength  $b_i$  that determines how much the fatigue influences the dynamics: this factor changes depending on neuro-modulation and explains the emergence of specific dynamic regimes associated to different brain states. Specifically, higher value of  $b$  (together with higher values of recurrent cortico-cortical connectivity) are used in models for the induction of Slow Oscillations.

It is possible to write down the dynamics for the activity variables by assuming that the probability at time  $t + dt$  to have a certain level of activity  $S_i(t + dt)$  in the population  $i$  is drawn from a Gaussian distribution:

$$p(S_i(t + dt) | \mathbf{S}(t)) = p(S_i(t + dt) | F_i(t)) = \frac{1}{\sqrt{2\pi c^2}} \exp \left[ -\frac{(S_i(t + dt) - F_i(t))^2}{2c^2} \right]. \quad (6)$$

For simplicity, we assumed  $c = 2s^{-1}$  to be constant in time, and the same for all the populations. Its temporal dynamics might be accounted for by considering a second order mean field theory [15, 11].

The average activity  $S_i(t + dt)$  of the population  $i$  at time  $t + dt$  is computed as a function of its input by using a leaky integrate and fire response function

$$\langle S_i(t + dt) \rangle = F[\mu_i(t), \sigma_i^2(t)] := F_i(t) \quad (7)$$

where  $F(\mu_i(t), \sigma_i^2(t))$  is the transfer function that, for an AdEx neuron under stationary conditions, can be analytically expressed as the flux of realizations (i.e., the probability current) crossing the threshold  $V_{spike} = \theta + 5\Delta V$  [48, 8]:

$$F(\mu) = F(\mu, \sigma^2 = \sigma_*^2) = \frac{1}{\sigma_*^2} \int_{-\infty}^{\theta + 5\Delta V} dV \int_{\max(V, V_r)}^{\theta + 5\Delta V} du e^{-\frac{1}{\tau_m \sigma_*^2} \int_V^u [f(v) + \mu \tau_m] dv}. \quad (8)$$

where  $f(v) = -(v(t) - E_l) + \Delta V e^{\frac{v(t) - \theta}{\Delta V}}$ ,  $\tau_m$  the membrane time constant,  $E_l$  the reversal potential,  $\theta$  the threshold,  $C$  the membrane capacitance,  $\Delta V$  the exponential slope parameter. The parameter values

Table 1: Neuronal parameters defining the two populations RS-FS model.

	$\theta$ (mV)	$\tau_m$ (ms)	$C$ (nF)	$V_r = E_l$ (mV)	$\Delta V$ (mV)	$\tau_i$ (ms)	$E_i$ (mV)	$b$ (nA)	$\tau_W$ (s)
exc	-50	20	0.2	-65	2.0	5	0	0.005	0.5
inh	-50	20	0.2	-65	0.5	5	-80	0	0.5

are reported in Table 1. Here we consider a small and constant  $\sigma_x^2 = 10^{-4}mV^2/s$ , since we assume small fluctuations, and that the fluctuations have a small effect on the population dynamics in any case. We will verify such assumption *a posteriori*. It is actually straightforward to work out the same theory without making any assumption on the size of  $\sigma$ , the only drawback is an increased computational power required to evaluate a 2D function (Eq. 8) during the inference (and simulation) procedure.

## The Inner Loop: likelihood maximization

It is possible to write the log-likelihood of one specific history  $\{S_i(t)\}$  of the dynamics of the model, given the parameters  $\{\xi_k\}$ , as follows:

$$L(\{S\}|\{\xi\}) = \sum_{it} \left[ -\frac{(S_i(t+dt) - F_i(t))^2}{2c^2} \right] \quad (9)$$

The optimal parameters, given an history of the system  $\{S(t)\}$ , can be obtained by maximizing the likelihood  $L(\{\xi_k\}|\{S\})$ . When using a gradient-based optimizer (we indeed use iR-prop) it is necessary to compute the derivatives that can be written as

$$\frac{\partial L(\{S\}|\{\xi\})}{\partial \xi_k} = - \sum_{it} \left[ \frac{(S_i(t+dt) - F_i(t))}{c^2} \right] \frac{\partial F_i(t)}{\partial \mu_i} \frac{\partial \mu_i}{\partial \xi_k} \quad (10)$$

where  $\frac{\partial F_i(t)}{\partial \mu_i}$  are computed numerically while  $\frac{\partial \mu_i}{\partial \xi_k}$  can be easily evaluated analytically. The value of  $c^2$  is not relevant since it can be absorbed in the learning rate.

The optimization procedure is performed independently on the 12 data chunks of 40s here considered. For each chunk, parameters are optimized on the first 32s while the remaining 8s are used for validation. The likelihood on such a dataset is evaluated with the inferred parameters, this is referred to as validation likelihood. It helps to prevent the risk of overfitting.

## Excitatory - Inhibitory module, the effective transfer function

In this paper, the single population (pixel) is assumed to be composed of two sub-populations of excitatory and inhibitory neurons; the mean of the input currents reads as:

$$\begin{cases} \mu_i^e(t) = \sum_k k_{ik}^{ee} S_k^e(t) + \sum_k k_{ik}^{ei} S_k^i(t) + I_{ext}^e - b_i W_i(t) \\ \mu_i^i(t) = \sum_k k_{ik}^{ie} S_k^e(t) + \sum_k k_{ik}^{ii} S_k^i(t) + I_{ext}^i \end{cases} \quad (11)$$

It is not always possible to distinguish the excitatory  $S^e$  from the inhibitory firing rates  $S^i$  in experimental recordings. Indeed, in electrical recordings the signal is a composition of the two activities. However, in our case we can make the assumption that the recorded activity, after the deconvolution, is a good proxy of the excitatory activity  $S^e$ . This is possible thanks to the fluorescent indicator we considered in this work, which targets specifically excitatory neurons. In this way, it is possible to constrain the excitatory activity and to consider  $S^i$  as hidden variable.

The transfer function depends both on the excitatory and the inhibitory activities  $F_e(S^e, S^i)$ . However,  $S^i$  is not observable in our dataset, and it is necessary to estimate an effective transfer function for the excitatory population of neurons by making an adiabatic approximation on the inhibitory one [27]. We define the effective transfer function as

$$F(S^e) = F_e^{eff}(S^e) = F_e(S^e, S^i(S^e)) \quad (12)$$

The inhibitory activity  $S^i$  is assumed to have a faster timescale. In first approximation a biologically plausible assumption when comparing the activity of FS (Fast Spiking) inhibitory neurons with RS (Regular Spiking) excitatory neurons. As a consequence  $S^i(S^e)$  can be evaluated as its stationary value given a fixed  $S^e$  value. The likelihood that contains this new effective transfer function is a function of  $k^{ee}$  and  $k^{ei}$ , which are the weights to be optimized. The dependence on  $k^{ie}, k^{ii}$  disappears, they have to be suitably chosen ( $k^{ie} = k^{ii} = -25$  in our case) and cannot be optimized with this approach.

## Elliptic exponentially-decaying connectivity kernels

Having a large number of parameters, especially in the case of small datasets, can cause convergence problems and can increase the risk of over-fitting. However, experimental constraints and priors can be used to reduce the number of parameters to be inferred. In our case we decided to exploit the information that the lateral connectivity decays with the distance, in first approximation according to a simple exponential reduction law [43], with long-range inter-areal connection suppressed during the expression of slow waves [32]. Furthermore, we supposed that a deformation from a circular symmetry to a more elliptical shape of the probability of connection could facilitate the creation of preferential directions of propagation. Therefore, we included this in the model as an exponential decay on the spatial scale  $\lambda$ . In this case the average input current to the population  $i$  can be written as already presented in Eq. 4, with  $k_{ik}$  taking into account the above discussed assumptions:

$$\mu_i(t) = \sum_k k_{ik} S_k(t) + I_{ext} - b_i W_i(t), \quad k_{ij} = k_0^j \exp\left(-\frac{d_{ij}}{\lambda_j}\right) \quad (13)$$

where  $d_{ik}$  is the distance between populations (i.e. pixels)  $i$  and  $k$ ,

$$d_{ik} = \rho_{ik} (1 + e_k \cos(2\theta_{ik} + 2\phi_k)) (1 + a_k \cos(\theta_{ik} + \phi_k)) \quad (14)$$

Parameters can be inferred by differentiating such parametrization of the connectivity kernel. For example, the derivative with respect to the spatial scale  $\lambda_k$  to feed eq.(10) would be:

$$\frac{\partial \mu_i(t)}{\partial \lambda_k} = k_{ik} S_k(t) \frac{d_{ik}}{\lambda_k^2} \quad (15)$$

## Gaussian Mixture Model

Collected the transition times to the up state in each of the  $L$  downsampled channels (44 and 41 informative channels for the two mice, respectively), each wave is hence described by a vector  $\mathbf{x}$  in a  $L$ -dimensional space. The problem of classifying slow waves into typical spatio-temporal patterns of propagation can then be tackled as a clustering problem in such high-dimensional space. We chose the approach based on Gaussian Mixture Model (GMM) [39].

We initially assumed  $K$  typical propagation patterns, each described by a  $L$ -dimensional multi-variate Gaussian, with its mean  $\boldsymbol{\mu}_k$  and covariance matrix  $\boldsymbol{\Sigma}_k$ . The probability of a wave  $\mathbf{x}_n$  to belong to the  $k$ -th category is hence given by the related multi-variate Gaussian density function:

$$p(\mathbf{x}_n | k) = \mathcal{N}(\mathbf{x}_n; \boldsymbol{\mu}_k, \boldsymbol{\Sigma}_k) \quad (16)$$

Ignoring which cluster each wave belongs to, one has to sum over all the possibilities, taking into account the relative weights  $\boldsymbol{\pi}$  of the  $K$  Gaussians in the *mixture*. The total likelihood for the set  $\mathbf{X}$  of waves hence reads:

$$p(\mathbf{X}) = \prod_{n=1}^N p(\mathbf{x}_n) = \prod_{n=1}^N \sum_{k=1}^K \pi_k \mathcal{N}(\mathbf{x}_n; \boldsymbol{\mu}_k, \boldsymbol{\Sigma}_k) \quad (17)$$

in fact depending on the set of Gaussian means and covariances  $\theta \equiv \{\boldsymbol{\mu}_k, \boldsymbol{\Sigma}_k\}$ ,  $p(\mathbf{X}) = p(\mathbf{X}; \theta)$ , as well as on the number  $K$  and the relative proportions  $\boldsymbol{\pi}$  of propagating modes.

The scope of this clustering procedure is in first place to infer the features of typical propagation patterns, i. e. their mean  $\boldsymbol{\mu}$  and their covariance  $\boldsymbol{\Sigma}$ . Then, each wave is assigned to one of these modes. To this aim, maximum-likelihood approaches are exploited, pointing at finding the optimal values of parameters  $\theta$  that maximize the likelihood  $\mathcal{L}(\theta) \equiv p(X; \theta)$  from Eq. (17). This can be easily attained through the python library *sklearn.mixture.GaussianMixture* [36], exploiting the Expectation-Maximization (EM) algorithm for likelihood maximization.

Notice that EM is guaranteed to converge to a local maximum of the likelihood. This implies that, for non-convex problems, the solution to which the algorithm converges depends on the initial condition. To get rid of this dependence, a possible strategy is to run the maximization by reshuffling the data and finally averaging over the final configurations of clusters.

In fact, the number of typical propagation patterns  $K$  is not even known *a priori*, so it has to be inferred as well. To face this problem, we run the above procedure for different numbers  $K$  of clusters and compare the resulting performances, exploiting a Gaussianity test (*scipy.stats.normaltest* [51]) as a quantitative parameter for comparison.

## Neuro-modulation

The periodic neuro-modulation we included in our network was modeled as a periodic oscillations of the parameters  $b$  and  $I^{ext}$  described by the following equations:

$$\begin{cases} I_i^{ext}(t) = I_i^{ext,0} \left( 1 + A \cos\left(\frac{2\pi t}{T}\right) \right) \\ b_i(t) = b_i^0 \left( 1 + \frac{A}{2} \cos\left(\frac{2\pi t}{T}\right) \right) \end{cases} \quad (18)$$

where we defined  $I_i^{ext,0}$  and  $b_i^0$  as the set of parameters inferred in the inner loop while  $A$  and  $T$  are the amplitude and the oscillation period optimized in the outer loop.

## The Outer Loop: grid search and data-simulation comparison

There can be different ways to define the outer loop. One way might be an iterative algorithm where at each step simulation and data are compared, and parameters are updated with some criterion. Here we use a simpler strategy, we implement a grid search of the parameters to be optimized, to find the best match between simulations and data. The parameters we considered are  $A$  and  $T$ , namely the amplitude and the period of the neuro-modulation (Eq. (18)). We run a  $10(T) \times 11(A)$  grid with parameter  $A$  linearly ranging from 0.2 to 4.0, and parameter  $T$  linearly ranging from 1.2s to 5s.

This choice was performed heuristically. However, it is possible to run a wider and denser grid search at the cost of a higher computational expense.

Thus, we process the simulation run over for each couple of values  $(a, p)$  in the grid search applying the same pipeline of analysis applied to experimental data, obtaining in output the distribution of the three previously defined local observables (see Section Slow Waves and Propagation analysis for more details): wave speed, propagation direction and inter wave interval. Then, we quantitatively compared each of these distributions with the ones observed in experimental data applying an Earth Mover's Distance (EMD) measure. Specifically, given two distributions  $u$  and  $v$ , EMD can be seen as the minimum amount of work (i.e. distribution weight that needs to be moved multiplied by the distance it has to be moved) required to transform  $u$  into  $v$ . In a more formal definition, EMD is also known as a Wasserstein distance between two 1D distributions, namely:

$$EMD(u, v) = \inf_{\pi \in \Gamma(u, v)} \int_{\mathbb{R} \times \mathbb{R}} |x - y| d\pi(x, y) = \int_{-\infty}^{+\infty} |U(s) - V(s)| \quad (19)$$

where  $\Gamma(u, v)$  is the set of (probability) distributions on  $\mathbb{R} \times \mathbb{R}$  whose marginals are  $u$  and  $v$  on the first and second factors respectively.  $U$  and  $V$  are the respective CDFs of  $u$  and  $v$ . The proof of the equivalence of

both definitions can be found in [38]. Specifically, for the purposes of this work, we evaluated the CDFs of each distribution sampling with a discrete binning. Moreover, in order to have this measure independent from the characteristic bin scale of the three studied observables, we evaluated EMD for speed, directions and IWI in "bin-unit": thanks to this approach, we can combine these measurements without incurring into non-homogeneous unit of measures inconsistencies. Specifically, to define a quantitative "score" describing the similarity between data and simulation, we chose to combine the three EMD computed over the three macroscopic local observables in and euclidian way, as follows:

$$EMD = \sqrt{EMD_{speed}^2 + EMD_{direction}^2 + EMD_{IWI}^2} \quad (20)$$

## Supporting information

### Slow Waves and Propagation analysis

To compare the simulation outputs with experimental data we implemented and applied the same analysis tools to both sets. Specifically, we improved the pipeline described by some of us in [9] to make it more versatile. First, experimental data are arranged to make them suitable for both the application of the slow wave propagation analysis and the inference method. Thus, data are loaded and converted into a standardized format; the region of interest is selected by masking channels of low signal intensity; fluctuations are further reduced applying a spatial downsampling: pixels are assembled in  $2 \times 2$  blocks through the function `scipy.signal.decimate` [51] curating the aliasing effect with the application of an ideal Hamming filter. Now data are ready to be both analyzed or given as input to the inference method.

Both experimental data and simulation output can then be given as input to these analysis tools. The procedure we followed is articulated into four blocks:

- Processing: the constant background signal is estimated for each pixel as the mean signal computed on the whole image set; it is then subtracted from images, pixel by pixel. Afterwards, the signal is filtered with a low-pass 4th order Butterworth filter at  $6Hz$ . The resulting signal is then normalized by its maximum.
- Trigger Detection: transition times from Down to Up states are detected. These are identified from the signal local minima. Specifically, the collection of transition times for each channel is obtained as the vertex of the parabolic fit of the minima.
- Wave Detection: the detection method used in [9] and described in [12] is applied. It consists in splitting the set of transition times into separate waves according to a *Unicity Principle* (i.e. each pixel can be involved in each wave only once) and a *Globality Principle* (i.e. each wave needs to involve at least 75% of the total pixel number).
- Wave Characterization: once that the wave collection has been identified, such set of waves is characterized by measuring local wave velocity, local wave direction and local SO frequency.

Specifically, we compute the local wave velocity as

$$v(x, y) = \frac{1}{|\nabla T(x, t)|} = \frac{1}{\sqrt{\left(\frac{\partial T(x, y)}{\partial x}\right)^2 + \left(\frac{\partial T(x, y)}{\partial y}\right)^2}} \quad (21)$$

where  $T(x, y)$  is the passage time function of each wave. Having access to this function only in the pixel discrete domain, the partial derivatives have been calculated as finite differences as follows:

$$\begin{cases} \frac{\partial T(x, y)}{\partial x} \simeq \frac{T(x + d, y) - T(x - d, y)}{2d} \\ \frac{\partial T(x, y)}{\partial y} \simeq \frac{T(x, y + d) - T(x, y - d)}{2d} \end{cases}$$

where  $d$  is the distance between pixels.

Concerning local directions, for each wave transition we compute a weighted average of wave local velocity components through a Gaussian filter  $w_{(\mu,\sigma)}$  centered in the pixel involved in the transition and with  $\sigma = 2$ . The local direction associated to the transition is

$$\theta(x, y) = \tan^{-1} \left( \frac{\langle v_y \rangle_{w_{(y,\sigma)}}}{\langle v_x \rangle_{w_{(x,\sigma)}}} \right) \quad (22)$$

Finally, the SO local frequency ( $f_{SO}$ ) is computed as the inverse time lag of the transition on the same pixel by two consecutive waves. Defining  $T^{(w)}(x, y)$  as the transition time of wave  $w$  on pixel  $(x, y)$ , the SO frequency can thus be computed as:

$$f_{SO}^{(1,2)}(x, y) = \frac{1}{T^{(2)}(x, y) - T^{(1)}(x, y)} \quad (23)$$

## A posteriori validation of simulated wave modes

*A posteriori* validation of simulated wave modes, for the two mice separately, is obtained comparing the optimal simulation with a control case obtained (shuffled simulation). The aim is to quantitatively show the statistical stability of obtained results.

We report the propagation modes identified by GMM fitted on the whole set of experimental waves only (3 identified modes, see Fig.7A,H), and the fraction of each identified mode (Fig.7D, K). We fit the GMM on the dataset composed of experimental waves and the corresponding simulated waves (Fig. 7 panels B and I, 4 modes are here identified). Looking at the occupancy of each of these modes (panels F and M, left) and comparing how it is distributed between data and simulation, it is worth noting that, for both mice, the three main modes identified are present in both data and simulation whereas a fourth mode (less frequent) is predominant in simulated datasets.

We replicated the same procedure on the dataset composed of experimental waves and the corresponding simulated waves, shuffling the latter through a channel permutation (equal for all simulated waves). Here, 4 modes are identified (Fig 7C and J), even if the occupancy distribution is much different from the previous scenario. As depicted in panels G and N, all experimental modes are described by only two of the identified modes and the predominant one is not populated by the shuffled simulated datasets. This, on the other hand, is described by 3 of the four modes identified, 2 of which are not occupied by experimental datasets.

To further expand this concept, we also compared the observed waves dynamics between experimental data, simulation and shuffled simulation (Fig 7 panels E and L). Specifically, we measured (left panels) the minimum euclidean distance in the channel space of each experimental wave from 1) simulated waves (black), 2) experimental waves -excluding itself- (blue) and 3) shuffled simulated waves (red); and vice versa (right panels). Through this procedure, we defined lower (2) and upper (3) bounds for the analysis, showing our experiment-simulation comparison lies within these bounds and specifically is closer to the self comparison rather than the shuffled scenario.

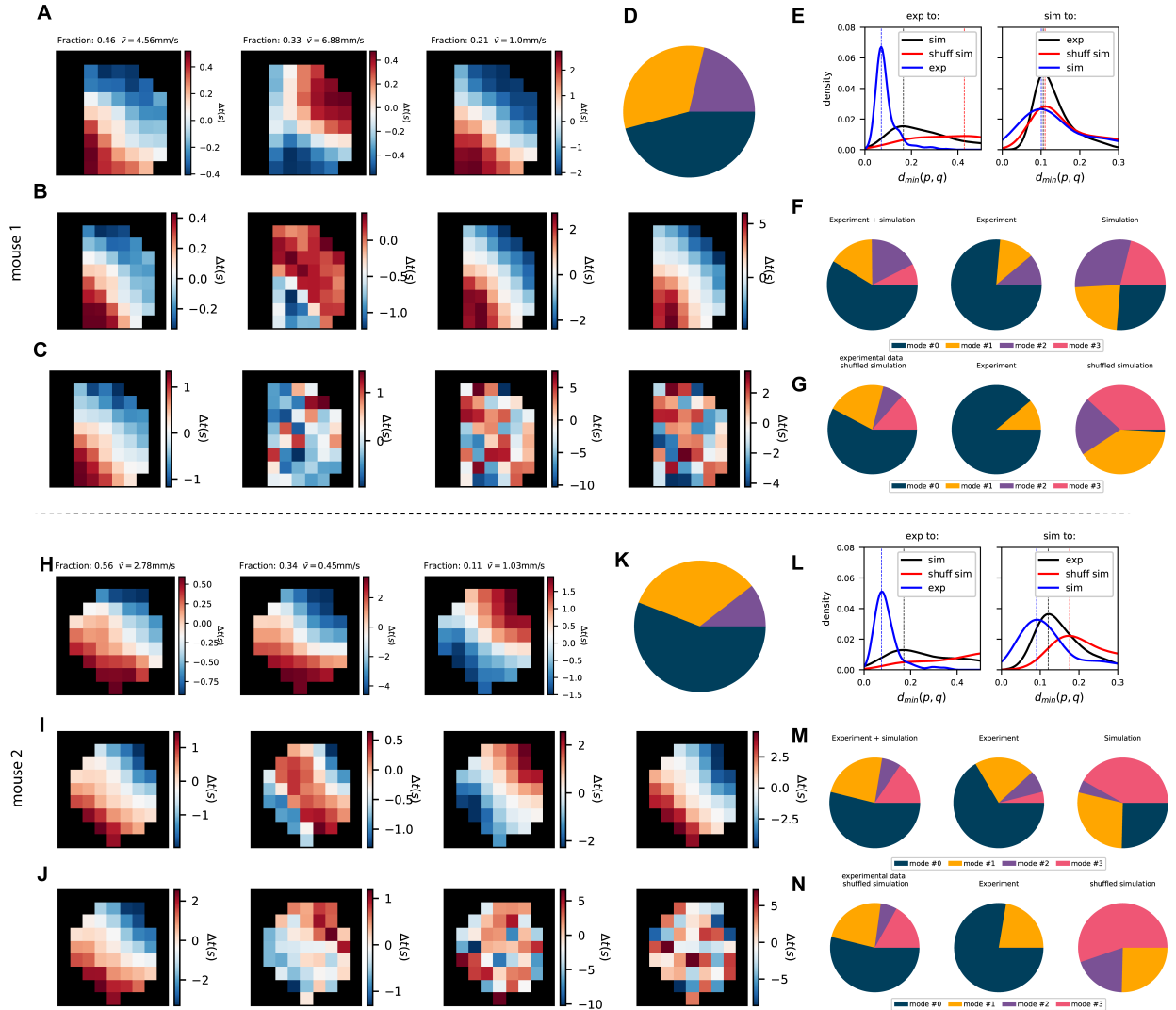


Figure 7: *A posteriori* validation of simulated wave modes, for the two mice separately, comparing the optimal simulation with a control case (shuffled simulation). **A,H.** Wave propagation modes identified by GMM fitted on experimental waves only (3 identified modes). **D, K.** Fraction of each identified mode. **B,I.** Wave propagation modes identified by GMM fitted on both experimental and simulated waves (4 identified modes). **F,M.** Fraction of each of the detected modes in the collection of both experimental and simulated waves (left), and in the sub-collections of experimental waves (center) and simulated waves (right). **C,J.** Wave propagation modes identified by GMM fitted on experimental and shuffled simulated waves (4 identified modes). **G,N.** Fractions of identified modes in the collection of both experimental and shuffled simulated waves (left), and in the sub-collections of experimental waves (center) and shuffled simulated waves (right). All the waves are shuffled through the same permutation of channels. **E, L.** Euclidean distances between experimental and simulated waves. Left: for each experimental wave, the minimum distance from simulated waves (black), the minimum distance from other experimental waves (blue, depicting a lower bound in the analysis) and the minimum distance from shuffled channel-wise simulated waves (red, depicting a higher bound in the analysis) are computed. Right: same procedure with inverted experimental and simulated waves. Dotted vertical lines depict the median of the distributions.

## Acknowledgments

This work has been supported by the European Union Horizon 2020 Research and Innovation program under the FET Flagship Human Brain Project (grant agreement SGA3 n. 945539 and grant agreement SGA2 n. 785907) and by the INFN APE Parallel/Distributed Computing laboratory.

## References

- [1] Walther Akemann et al. “Imaging neural circuit dynamics with a voltage-sensitive fluorescent protein”. In: *Journal of neurophysiology* 108.8 (2012), pp. 2323–2337.
- [2] Marco Aqil et al. “Graph neural fields: A framework for spatiotemporal dynamical models on the human connectome”. In: *PLOS Computational Biology* 17.1 (Jan. 2021), pp. 1–29. DOI: 10.1371/journal.pcbi.1008310. URL: <https://doi.org/10.1371/journal.pcbi.1008310>.
- [3] Cristiano Capone, Guido Gigante, and Paolo Del Giudice. “Spontaneous activity emerging from an inferred network model captures complex spatio-temporal dynamics of spike data”. In: *Scientific reports* 8.1 (2018), p. 17056.
- [4] Cristiano Capone and Maurizio Mattia. “Speed hysteresis and noise shaping of traveling fronts in neural fields: role of local circuitry and nonlocal connectivity”. In: *Scientific reports* 7.1 (2017), pp. 1–10.
- [5] Cristiano Capone et al. “Inferring synaptic structure in presence of neural interaction time scales”. In: *PloS one* 10.3 (2015), e0118412.
- [6] Cristiano Capone et al. “Sleep-like slow oscillations improve visual classification through synaptic homeostasis and memory association in a thalamo-cortical model”. In: *Scientific Reports* 9.1 (2019), p. 8990.
- [7] Cristiano Capone et al. “Slow waves in cortical slices: how spontaneous activity is shaped by laminar structure”. In: *Cerebral cortex* 29.1 (2019), pp. 319–335.
- [8] Cristiano Capone et al. “State-dependent mean-field formalism to model different activity states in conductance-based networks of spiking neurons”. In: *Physical Review E* 100.6 (2019), p. 062413.
- [9] Marco Celotto et al. “Analysis and model of cortical slow waves acquired with optical techniques”. In: *Methods and protocols* 3.1 (2020), p. 14.
- [10] Tsai-Wen Chen et al. “Ultrasensitive fluorescent proteins for imaging neuronal activity”. In: *Nature* 499.7458 (2013), pp. 295–300.
- [11] Meng Nan Chong et al. “Recent developments in photocatalytic water treatment technology: a review”. In: *Water research* 44.10 (2010), pp. 2997–3027.
- [12] Giulia De Bonis et al. “Analysis Pipeline for Extracting Features of Cortical Slow Oscillations”. In: *Frontiers in Systems Neuroscience* 13 (2019), p. 70. ISSN: 1662-5137. DOI: 10.3389/fnsys.2019.00070. URL: <https://www.frontiersin.org/article/10.3389/fnsys.2019.00070>.
- [13] Brian DePasquale et al. “full-FORCE: A target-based method for training recurrent networks”. In: *PloS one* 13.2 (2018), e0191527.
- [14] Matteo Di Volo et al. “Biologically realistic mean-field models of conductance-based networks of spiking neurons with adaptation”. In: *Neural computation* 31.4 (2019), pp. 653–680.
- [15] Sami El Boustani and Alain Destexhe. “A master equation formalism for macroscopic modeling of asynchronous irregular activity states”. In: *Neural computation* 21.1 (2009), pp. 46–100.
- [16] Erik D Fagerholm et al. “Cortical entropy, mutual information and scale-free dynamics in waking mice”. In: *Cerebral cortex* 26.10 (2016), pp. 3945–3952.
- [17] Guido Gigante, Maurizio Mattia, and Paolo Del Giudice. “Diverse population-bursting modes of adapting spiking neurons”. In: *Physical Review Letters* 98.14 (2007), p. 148101.
- [18] Jennifer S. Goldman et al. “Bridging Single Neuron Dynamics to Global Brain States”. In: *Frontiers in Systems Neuroscience* 13 (2019), p. 75. ISSN: 1662-5137. DOI: 10.3389/fnsys.2019.00075. URL: <https://www.frontiersin.org/article/10.3389/fnsys.2019.00075>.

- [19] Bruno Golosio et al. “Thalamo-cortical spiking model of incremental learning combining perception, context and NREM-sleep”. In: *PLoS Computational Biology* 17.6 (2021), e1009045.
- [20] Anastasia Greenberg et al. “New waves: Rhythmic electrical field stimulation systematically alters spontaneous slow dynamics across mouse neocortex”. In: *Neuroimage* 174 (2018), pp. 328–339.
- [21] Christine Grienberger and Arthur Konnerth. “Imaging calcium in neurons”. In: *Neuron* 73.5 (2012), pp. 862–885.
- [22] Robin Gutzen et al. “Building adaptable and reusable pipelines for investigating the features of slow cortical rhythms across scales, methods, and species”. In: Bernstein Conference, online (Germany), 29 Sep 2020 - 29 Oct 2020. Sept. 29, 2020. DOI: 10.12751/NNCN.BC2020.0030. URL: <https://juser.fz-juelich.de/record/885608>.
- [23] Christian Igel and Michael Hüsken. “Empirical evaluation of the improved Rprop learning algorithms”. In: *Neurocomputing* 50 (2003), pp. 105–123.
- [24] Christian Igel and Michael Hüsken. “Improving the Rprop learning algorithm”. In: *Proceedings of the second international ICSC symposium on neural computation (NC 2000)*. Vol. 2000. Citeseer. 2000, pp. 115–121.
- [25] Pinggan Li et al. “Measuring sharp waves and oscillatory population activity with the genetically encoded calcium indicator GCaMP6f”. In: *Frontiers in cellular neuroscience* 13 (2019), p. 274.
- [26] Guillaume Marrelec et al. “Functional Connectivity’s Degenerate View of Brain Computation.” In: *PLoS Computational Biology* 12(10): e1005031 (2016). ISSN: 1553-7358. DOI: 10.1371/journal.pcbi.1005031. URL: <https://journals.plos.org/ploscompbiol/article?id=10.1371/journal.pcbi.1005031>.
- [27] Massimo Mascalzo and Daniel J Amit. “Effective neural response function for collective population states”. In: *Network: Computation in Neural Systems* 10.4 (1999), pp. 351–373.
- [28] Francesca Melozzi et al. “Individual structural features constrain the mouse functional connectome”. In: *Proceedings of the National Academy of Sciences* 116.52 (2019), pp. 26961–26969. ISSN: 0027-8424. DOI: 10.1073/pnas.1906694116. eprint: <https://www.pnas.org/content/116/52/26961.full.pdf>. URL: <https://www.pnas.org/content/116/52/26961>.
- [29] Majid H Mohajerani et al. “Spontaneous cortical activity alternates between motifs defined by regional axonal projections”. In: *Nature neuroscience* 16.10 (2013), p. 1426.
- [30] Paolo Muratore, Cristiano Capone, and Pier Stanislao Paolucci. “Target spike patterns enable efficient and biologically plausible learning for complex temporal tasks”. In: *PloS one* 16.2 (2021), e0247014.
- [31] Trang-Anh Nghiem et al. “Maximum-entropy models reveal the excitatory and inhibitory correlation structures in cortical neuronal activity”. In: *Physical Review E* 98.1 (2018), p. 012402.
- [32] Umberto Olcese et al. “Spike-Based Functional Connectivity in Cerebral Cortex and Hippocampus: Loss of Global Connectivity Is Coupled to Preservation of Local Connectivity During Non-REM Sleep”. In: *Journal of Neuroscience* 36.29 (2016), pp. 7676–7692. ISSN: 0270-6474. DOI: 10.1523/JNEUROSCI.4201-15.2016. eprint: <https://www.jneurosci.org/content/36/29/7676.full.pdf>. URL: <https://www.jneurosci.org/content/36/29/7676>.
- [33] Il Memming Park et al. “Encoding and decoding in parietal cortex during sensorimotor decision-making”. In: *Nature neuroscience* 17.10 (2014), pp. 1395–1403.
- [34] Elena Pastorelli et al. “Scaling of a Large-Scale Simulation of Synchronous Slow-Wave and Asynchronous Awake-Like Activity of a Cortical Model With Long-Range Interconnections”. In: *Frontiers in Systems Neuroscience* 13 (2019), p. 33. ISSN: 1662-5137. DOI: 10.3389/fnsys.2019.00033. URL: <https://www.frontiersin.org/article/10.3389/fnsys.2019.00033>.
- [35] Antonio Pazienti et al. “Slow waves form expanding, memory-rich mesostates steered by local excitability in fading anesthesia”. In: *Isience* 25.3 (2022), p. 103918.
- [36] F. Pedregosa et al. “Scikit-learn: Machine Learning in Python”. In: *Journal of Machine Learning Research* 12 (2011), pp. 2825–2830.

- [37] Jonathan W Pillow et al. “Spatio-temporal correlations and visual signalling in a complete neuronal population”. In: *Nature* 454.7207 (2008), pp. 995–999.
- [38] Aaditya Ramdas, Nicolas Garcia, and Marco Cuturi. *On Wasserstein Two Sample Testing and Related Families of Nonparametric Tests*. 2015. DOI: 10.48550/ARXIV.1509.02237. URL: <https://arxiv.org/abs/1509.02237>.
- [39] Douglas A Reynolds. “Gaussian mixture models.” In: *Encyclopedia of biometrics* 741.659-663 (2009).
- [40] Vahid Rostami et al. “Bistability, non-ergodicity, and inhibition in pairwise maximum-entropy models”. In: *PLoS computational biology* 13.10 (2017), e1005762.
- [41] Yasser Roudi, Benjamin Dunn, and John Hertz. “Multi-neuronal activity and functional connectivity in cell assemblies”. In: *Current opinion in neurobiology* 32 (2015), pp. 38–44.
- [42] Elad Schneidman et al. “Weak pairwise correlations imply strongly correlated network states in a neural population”. In: *Nature* 440.7087 (2006), pp. 1007–1012.
- [43] Philipp Schnepel et al. “Physiology and Impact of Horizontal Connections in Rat Neocortex”. In: *Cerebral Cortex* 25.10 (Nov. 2014), pp. 3818–3835. ISSN: 1047-3211. DOI: 10.1093/cercor/bhu265. eprint: <https://academic.oup.com/cercor/article-pdf/25/10/3818/14101924/bhu265.pdf>. URL: <https://doi.org/10.1093/cercor/bhu265>.
- [44] Gregory Scott et al. “Voltage imaging of waking mouse cortex reveals emergence of critical neuronal dynamics”. In: *Journal of Neuroscience* 34.50 (2014), pp. 16611–16620.
- [45] Daisuke Shimaoka, Chenchen Song, and Thomas Knöpfel. “State-dependent modulation of slow wave motifs towards awakening”. In: *Frontiers in cellular neuroscience* 11 (2017), p. 108.
- [46] *Slow Wave Analysis Pipeline (SWAP): Integrating multi-scale data and the output of simulations in a reproducible and adaptable pipeline*. <https://wiki.ebrains.eu/bin/view/Collabs/slow-wave-analysis-pipeline>. Accessed: 2021-04-14.
- [47] Giulio Tononi, Olaf Sporns, and Gerald M. Edelman. “Measures of degeneracy and redundancy in biological networks”. In: *Proceedings of the National Academy of Sciences* 96.6 (1999), pp. 3257–3262. ISSN: 0027-8424. DOI: 10.1073/pnas.96.6.3257. eprint: <https://www.pnas.org/content/96/6/3257.full.pdf>. URL: <https://www.pnas.org/content/96/6/3257>.
- [48] Henry C Tuckwell. *Introduction to theoretical neurobiology: volume 2, nonlinear and stochastic theories*. Vol. 8. Cambridge University Press, 1988.
- [49] Joanna Tyrcha et al. “The effect of nonstationarity on models inferred from neural data”. In: *Journal of Statistical Mechanics: Theory and Experiment* 2013.03 (2013), P03005.
- [50] Matthieu P Vanni et al. “Mesoscale mapping of mouse cortex reveals frequency-dependent cycling between distinct macroscale functional modules”. In: *Journal of Neuroscience* 37.31 (2017), pp. 7513–7533.
- [51] Pauli Virtanen et al. “SciPy 1.0: Fundamental Algorithms for Scientific Computing in Python”. In: *Nature Methods* 17 (2020), pp. 261–272. DOI: 10.1038/s41592-019-0686-2.
- [52] Alison I Weber and Jonathan W Pillow. “Capturing the dynamical repertoire of single neurons with generalized linear models”. In: *Neural computation* 29.12 (2017), pp. 3260–3289.
- [53] Patrick W Wright et al. “Functional connectivity structure of cortical calcium dynamics in anesthetized and awake mice”. In: *PloS one* 12.10 (2017), e0185759.
- [54] Yicheng Xie et al. “Resolution of high-frequency mesoscale intracortical maps using the genetically encoded glutamate sensor iGluSnFR”. In: *Journal of Neuroscience* 36.4 (2016), pp. 1261–1272.